Optics & Laser Technology 161 (2023) 109148

Contents lists available at ScienceDirect

Optics and Laser Technology

journal homepage: www.elsevier.com/locate/optlastec

Full length article

FEA based opto-mechanisms design and thermal analysis of a dynamic SFS with an ultra-long exit pupil distance

Yue Pan [a,*], Kailin Zhang [a,*], Mai Hu [b], Yuanming Zhao [c], Xiping Xu [a]

[a] College of Optoelectronic Engineering, Changchun University of Science and Technology, 7089 Wei Xing Road, Changchun 130022, China
[b] Changchun Institute of Optics, Fine Mechanics and Physics, Chinese Academy of Sciences, 3888 Dong Nanhu Road, Changchun 130022, China
[c] The 27th Research Institute of China Electronics Technology Group Corporation, 36 Boxue Road, Zhengzhou 470000, China

ARTICLE INFO

Keywords:
Instrumentation, measurement, and metrology
Optical instruments
Optomechanics
Surface measurements
Thermal effects

ABSTRACT

The dynamic star field simulator (SFS) reproduces the actual operating conditions for the star tracker (STR) to assess its performance along with the flight motion simulator (FMS) in the hard-ware-in-the-loop (HWIL) simulation. The exit pupil distance of a traditional SFS is extremely short, which limits its application to large FMSs. To project the liquid crystal on silicon (LCoS) output to the STR entrance pupil, a 1250 mm ultra-long exit pupil distance SFS, operating in the broad waveband of 450–900 nm, is designed and implemented. In this study, the opto-mechanisms design and thermal analysis of the SFS are evaluated. The detailed design for key assemblies is specifically addressed to suppress negative heat effects. From the finite element analysis (FEA) results under different thermal conditions, the Zernike coefficients of 16 deformed optical surfaces in the projection module are solved using singular value decomposition (SVD), and the temperature adaptability is verified using a ray-tracing software. The preliminary SFS assessment confirms the simplicity of manufacture and excellent performance. The closed-loop opto-mechanisms design significantly improves the SFS reliability and enhances its suitability for large FMS use.

1. Introduction

The star field simulator (SFS) is extensively used for testing and evaluation in the aerospace industry to determine the attitude accuracy of a star tracker (STR) during hardware-in-the-loop (HWIL) tests [1,2]. It is essentially a “pupil to pupil” projector, similar to an infrared scene projector (IRSP) but different to a solar simulator, as the latter focuses on the accuracy of simulated spectrums [3]. These projectors are usually divided into two categories: static and dynamic. The static SFS uses fiber optics or a star test plate to generate static artificial stars [4]. The dynamic SFS uses a scene generation device (SGD) to provide star patterns, which provides more robust STR testing [5,6]. Three typical SGDs are generally selected in an SFS or projection display—a liquid crystal display (LCD), a digital micro-mirror device (DMD), and liquid crystal on silicon (LCoS).

LCD is a transmissive spatial light modulator, using the electro-optic effect to produce a gray image. Jena Optronik developed the Optical Sky field Simulator (OSI) to evaluate the STR used for the second SHarp Edge Flight Experiment (SHEFEX-2) [7]. The device has a micro display with an 800 × 600 pixel resolution and a 60 Hz frame rate, where the theoretical single star accuracy is 0.0033°. The American Jet Propulsion Laboratory (JPL) designed a similar SFS to test CubeSat-scale star trackers [8]. A computer LCD screen is used to show the star field in the test facility “Federico II” at Naples University, which makes the system extremely heavy and bulky [9]. The three SFSs have a short exit pupil distance, particularly for the OSI directly attached to the STR. Accordingly, they are incompatible with the large flight motion simulator (FMS). Considering this limitation, Changchun Institute of Optics, Fine Mechanics and Physics designed the LCD-based visible scene simulator with a 700 mm exit pupil distance [10].

A DMD consists of a micromirror array, controlled by pulse width modulation (PWM) technology to generate a gray image. Compared with LCD, the significant advantage of DMDs is the high spectral response (only depending on the window material). Therefore, DMDs are widely used in the fields of commercial projection and optical HWIL simulation. However, the single star accuracy relies on the smaller pixel size, which causes diffraction of the broad waveband, leading to stray light [11–14]. As for the optical engine, the prism or the field lens is usually used to separate the illumination and projection beams. Chengdu Institute of Optics and Electronics designed a DMD-based SFS

* Corresponding authors.
E-mail addresses: panyue@cust.edu.cn, zhangkailin@mails.cust.edu.cn (K. Zhang).

https://doi.org/10.1016/j.optlastec.2023.109148
Received 9 June 2022; Received in revised form 6 January 2023; Accepted 7 January 2023
Available online 17 January 2023

with a 28.6° field of view and a 60 mm exit pupil distance, using a total internal reflection (TIR) prism [15].

Furthermore, the prisms have also been adopted by the National Central University and National Chiao Tung University to design compact projectors [16,17]. Shanghai Institute of Technical Physics used a mirror and a field lens to design an optical engine. However, the field lens was shared by both illumination and projection, complicated by the suppression of stray light [18,19]. In addition, an IRSP was designed using direct lighting, which is unsuitable for the design proposed in this study, owing to the requirement of a long back working distance for projection and illumination [20].

LCoS combines the advantages of DMD and LCD, having a higher contrast, optical efficiency, and fill factor and smaller pixel size, which extend the star field projection capability. Furthermore, its optical engine design is also simpler than DMDs [21,22]. Changchun University of Science and Technology designed a two-LCoS-based SFS to obtain a larger field of view and higher spatial resolution. The splicing method can achieve a field of view of more than 30°. However, the exit pupil distance is still less than 100 mm, which limits its application in HWIL simulations [23,24]. Additionally, Zhejiang University developed a CF-LCoS pico-projector, which uses double freeform lenses to replace traditional integrators, significantly compressing the volume of the projector. However, the commercial projector is more concerned with the visual experience parameters, such as the chromaticity and the throw ratio, and does not meet the "pupil to pupil" test requirements of the STR [25].

For the thermal analysis, the transmissive-type projector is more challenging to assess than the reflective-type imaging system, owing to the on-axis heat source and excessive number of optical surfaces. Even if the projection and illumination are analyzed separately according to different thermal loadings, the temperature adaptability of projector cannot be accurately evaluated [26]. However, the current studies primarily focus on the reflective-type imaging system, usually stressing the analysis of structure deformation under special conditions, rather than the deformation induced optical performance degradation [27,28]. In some cases, only the primary mirror assembly is analyzed and optimized [29,30].

In this study, a novel LCoS-based SFS is designed and built, with the advantages of a broad waveband and an ultra-long exit pupil distance. Compared with the previous designs, the SFS is more suitable for use with a large FMS. Furthermore, an optimized opto-mechanics closed-loop design based on FEA is presented to avoid the negative influence of heat on optical performance. For the projection lens, Zernike coefficients of 16 deformed optical surfaces are solved using singular value decomposition (SVD) method. A comparative analysis of the optical performance is conducted using ray-tracing software for different ambient temperatures. The findings of this study emphasize the feasibility of SFS, popularizing the closed loop opto-mechanics design method for application in other similar systems.

The rest of the paper is organized as follows. The operating principle of the SFS and the optical design result are presented in Section II. The opto-mechanics design is then discussed in detail in Section III. The thermally induced deformation of the optical surface is analyzed using FEA in Section IV. The laboratory-based preliminary tests and calibrations are provided in Section V.

2. Operating principle and optical design

The process of the HWIL simulation tests of the STR is depicted in Fig. 1. The simulation controller converted the star field image into a video signal that was uploaded to the SFS. Further, the SFS generated and projected the image to the entrance pupil of the STR. The STR under test analyzed the received image to make a judgement and sent corresponding instructions to the simulation controller, which controlled the movement of the FMS to adjust the flight attitude of the STR. In this process, the SFS moved simultaneously with the STR, and they remained

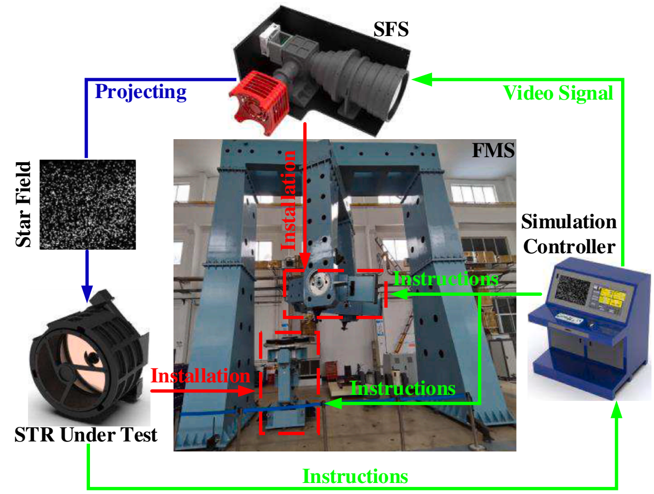

Fig. 1. Process of HWIL simulation tests of the STR.

in a relatively static state to make the pupils coincide. The SFS and STR were separately installed on an azimuth/elevation gimbal and a two-axis platform. To avoid collision, the exit pupil distance of the SFS was 1250 mm, and the size of the pupil was greater than 45 mm to cover the entrance pupil of the STR. The waveband of the SFS was 450–900 nm ranging from visible to near-infrared, to match the STR. As a testing instrument, the distortion of the optical engine was less than 0.5 % under all fields of view, to increase the accuracy of the star point position. These features present new challenges for the design of the SFS. The design specifications are listed in Table 1.

The configuration of the SFS optical engine is depicted in Fig. 2. The polarized-beam splitter (PBS) prism primarily reflected the s-polarized light required by the LCoS chip and transmitted the p-polarized light absorbed by the stray light trap to prevent the beam from returning. The stray light trap was bound to the inner surfaces of the prism housing, which was made of light absorbing material with an absorption rate of 99.9 % in the waveband of 0.3–14 μm. It is worth noting that the polarizing efficiency of a PBS prism varies with the illumination numerical aperture (NA). With the increase in NA, an increased amount of p-polarized light existed in the reflected beam to reduce the contrast. Furthermore, the illumination NA was greater than the projection such that the energy modulated by LCoS filled the entrance pupil of the projection lens. A clean-up polarizer or an input pre-polarizer was required for the system with fast F/# to improve the contrast.

The illumination exit pupil was set on the LCoS surface coinciding with the projection entrance pupil. The cone angle of the output beam of the light source was ± 60°, thus, a condenser lens with two aspheric surfaces was used to collect the energy and reduce the cone angle of the beam. Two multi-lens arrays placed back-to-back were used to shape the exit spot into a rectangle and significantly improve lighting uniformity. If the spot was not shaped, at least 38 % of the energy would be wasted,

Table 1
Design Specifications and Performance.

Parameter	Value
Spectral ranges	400 nm–900 nm
Field of view	≥±2°
Exit pupil relief	≥1250 mm
Exit pupil diameter	≥Φ45mm
Single star position error	≤20″
Angular distance error between stars	≤15″
Video interface	Display port (DP)
Spatial resolution of LCoS	2048 × 1536
Pixel pitch of LCoS	8.3 μm
Active area of LCoS	17 × 12.7 mm

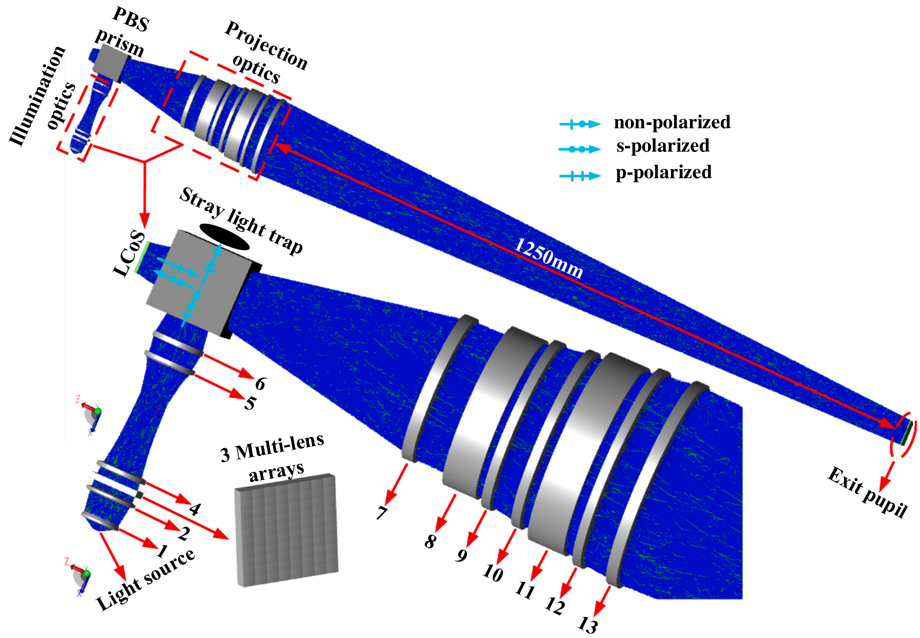

Fig. 2. Projection optical engine of the SFS. The polarization state of the beam will change after modulation by LCoS. Lens 1 denotes the condenser lens. Lens 2 collimates the beam. Lenses 4–6 comprise the Kohler lighting architecture. Lenses 7–13 comprise the projection optics.

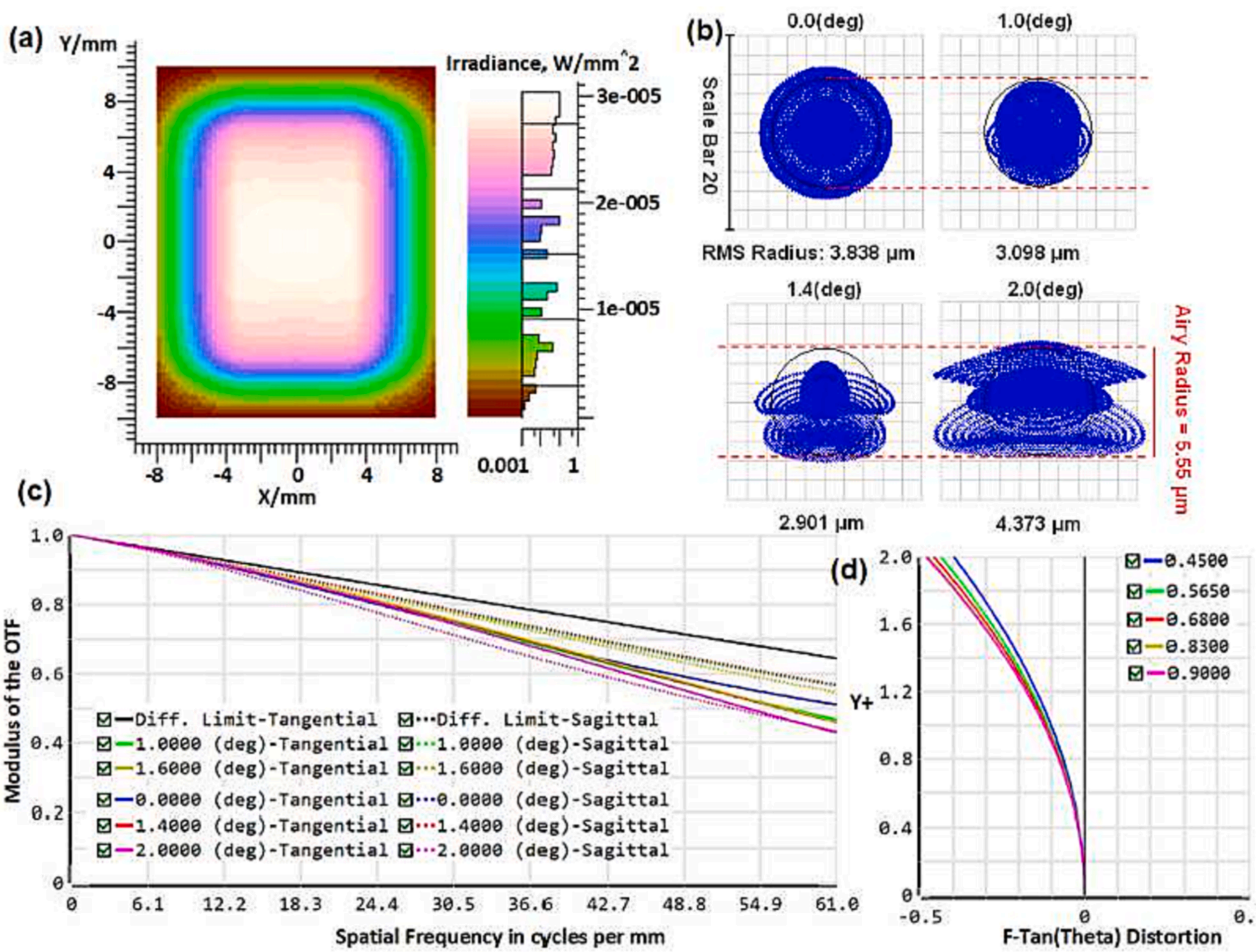

Fig. 3. Optical design result. (a) Irradiance chart of LCoS active area. (b) Projection spot diagram. (c) Projection MTF curves. (d) Projection distortion curves.

which would result in a serious decline in contrast and optical efficiency. Finally, the output beam through the arrays was imaged on the focal plane of the front group of lenses to comprise Kohler lighting architecture.

As the F/# of the projection optics was 6.68, the illumination NA of the image space was set to 0.1045 which was sufficient. The transmission of p-polarized light can be greater than 90 % under this NA. Therefore, there was no auxiliary polarizer in the SFS, which also reduced the difficulty of assembly and alignment. To meet the demand of the exit pupil position, the incident height of the projection beam was increased. Consequently, the diameter of lens 13 was up to 138 mm, and other lenses were also greater than 100 mm in diameter. Furthermore, the increased incident height and wide waveband presented difficulties in correcting distortion and chromatic aberrations [31]. Considering the design specifications and aberration characteristics comprehensively, the final optimized result of optical engine is shown in Fig. 2.

The active area of LCoS was divided into 15 × 11 units, and the illuminance chart is shown in Fig. 3(a). Based on obtaining the illuminance value of each unit, the uniformity was calculated by:

$$U = 1 - \sqrt{\sum_{i=1}^{165} \left(E_i - \overline{E}\right)^2 / 165} / \overline{E} \tag{1}$$

where E_i is the illuminance of each unit, and $\overline{E}$ is the average of the illuminance. The result showed that the illuminance uniformity was greater than 0.87, and there was no significant difference between the X and Y directions. The projection spot diagram is shown in Fig. 3(b), where the airy radius is 5.55 μm, and the maximum RMS radius of all fields is 4.373 μm, which is smaller than the airy radius and close to the pixel size. Considering the practical demand of the magnitude, more than 4 pixels were required to display a star point. When the radius was 8 μm, the diffraction encircled energy was greater than 82 %. The modulation transfer function (MTF) curves shown in Fig. 3(c) imply that the values of the modulus were greater than 0.4 at 61 cycles per mm (C/mm). In addition, it can be seen from Fig. 3(d) that the distortion values were less than 0.5 %, which improved the accuracy of the star point position.

3. Opto-mechanisms design of the SFS

The detailed configuration and cross-section of the SFS are presented in Fig. 4. The prism leaned against three pads to achieve the positioning. Further, the prism was bonded to its base by an epoxy optical adhesive (two-component). These precision machined pads only provided a plane along the X or Y direction and had no additional effect on the prism. Due to the long distance (125 mm) between lens 7 and the prism, the barrel of the projection lens was constructed in two parts joined by a piloted interface with a flange. The spacer between the two parts was primarily used to control the tilt and the axial air spacing of the prism, with a small amount of decentration allowed. Each element or group of elements was centered and bonded to the cell. After curing, the individual cell-lens subassembly was sequentially inserted into the corresponding barrel and held securely by the retaining ring.

During the SFS test, it was found that there was a clear ringlike spot on the projection image, which was not anticipated in the design process. If lens 7 is regarded as the detector, most of the inner surfaces of the barrel could be critical surfaces observable by the detector. If a critical surface is illuminated, the stray light will pass through the lens and affect the projection image quality. As the connection barrel was manufactured, there was no way to directly add stray light elimination structures on the inner surface. The solution was that extra seven vanes were inserted into the barrel, the goal of which was to block all first-order stray light paths without interrupting the normal light path. The initial design consisted of an entrance aperture (64 mm), the effective aperture of lens 7 as a detector (90.8 mm), and the distance between them. The method proposed in reference [32] was adopted to determine the positions of vanes. It is worth noting that the connection barrel was regarded as the main baffle used in the imaging system in the vane design process. The bevel angle of the vane was set as 45° for ease of fabrication. To prevent the bevel of the vane from being critical, the bevels of the first six vanes were oriented to face outward. However, the last vane was oriented to face inward to prevent its bevel from being illuminated. After adjusting vane positions, they were locked in the final position and bound to the barrel.

The stray light suppression ability of the opto-mechanical model was evaluated by non-sequence ray tracing. The active area of LCoS was set as the Lambert light source, which was different from the imaging system. The angle of the exit beam of the source was set to be larger than

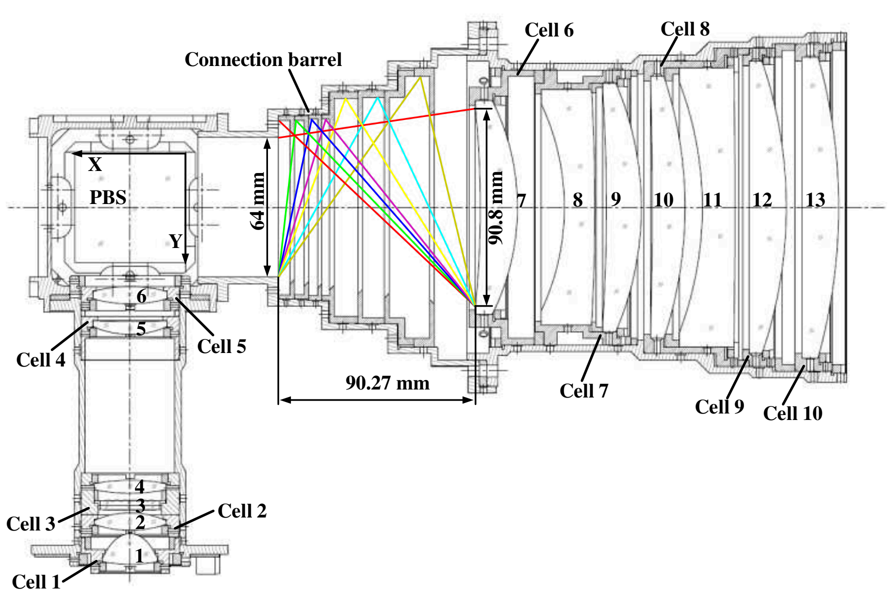

Fig. 4. Detailed configuration and cross-section of the SFS. All axes are coplanar. The color lines are construction lines and vanes are placed at the intersection points between the lines with the same color.

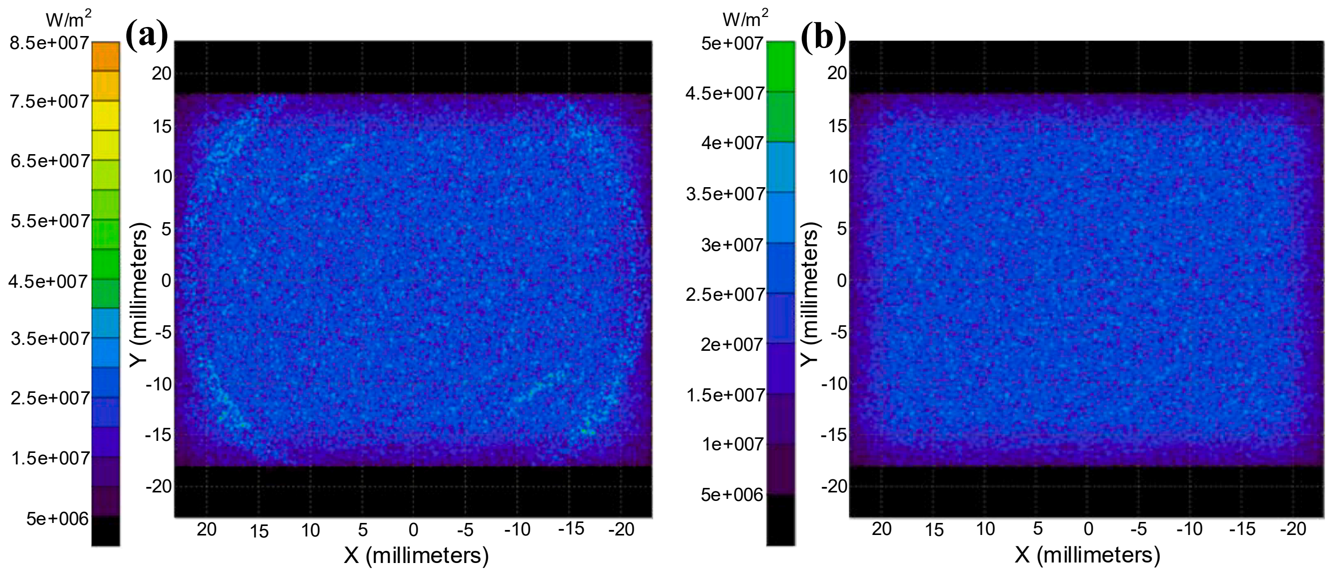

Fig. 5. Irradiance map of the receiving surface. (a) Barrel with no vanes. (b) Barrel with vanes.

the real aperture angle of the projection beam, resulting in stray light. The aspect ratio of the receiving surface was 4:3, which was slightly larger than the actual size. During the simulation, 900,000 rays were traced, and the irradiance map of the receiving surface is shown in Fig. 5. The area with higher brightness is the actual exit pupil surface. Comparing the barrels with and without vanes, it shows that the stray light suppression ability of the SFS was effectively improved by vanes.

Tolerances were determined based on the feasibility and accuracy of the manufacturing and alignment [33]. Tolerance analyses of the projection and illumination lenses focused on the image quality and illuminance uniformity, respectively. The results revealed that the error of axial air spacing was less than 0.03 mm, the decentration was 0.02 mm, and the tilt was 48″. In addition, the wedge angles of the front surfaces of lenses 7 and 9 were 48″ and that of the rest of the elements were 42″. The tolerances are acceptable and readily achieved by the centering technique. Considering these tolerances, the MTF values of the SFS decreased by a maximum of 16 %, which indicates that the SFS can be easily built.

The mechanical parts and optical elements were fabricated and tested to meet the designed tolerances. The assembly processes for illumination and projection lenses were similar. All the optical elements had their own cells, and the cell radius was 0.5 mm smaller than the inner radius of the corresponding position of the lens barrel. The cell relied on precisely machined shoulders inside the lens barrel for positioning. When one cell was moved to the specified position, the decentration of the lens assembled inside the cell was adjusted with screws. The axial air spacing and the tilt were adjusted by correcting the spacer between the cells. The spacer was made of aluminum (2A12), which was easy to further process during assembly and alignment. The prism housing and its square base were machined in pairs to achieve a 1′ parallelism between the prism surface and the mounting surface of the housing. Meanwhile, the prism subassembly also served as the compensator for the projection lens. In addition to correcting the spherical aberration, controlling the axial air spacing between the prism and lens 7 improved the image quality. In summary, the assembly and alignment of the SFS were conducted under the monitoring of the centering device, as shown in Fig. 6(a), to obtain the desired tolerances.

The overall system is shown in Fig. 6(b). The projection and illumination subassemblies were connected with the prism housing by a flange structure. The LCoS was assembled on the rear mounting surface of the prism housing. Furthermore, there was a shim between them to adjust the position of the LCoS. The illumination and prism subassemblies were installed on the base together. Both the prism housing and the base were machined from one solid, and all the mounting surfaces were precision-machined to achieve the desired parallelism or perpendicularity.

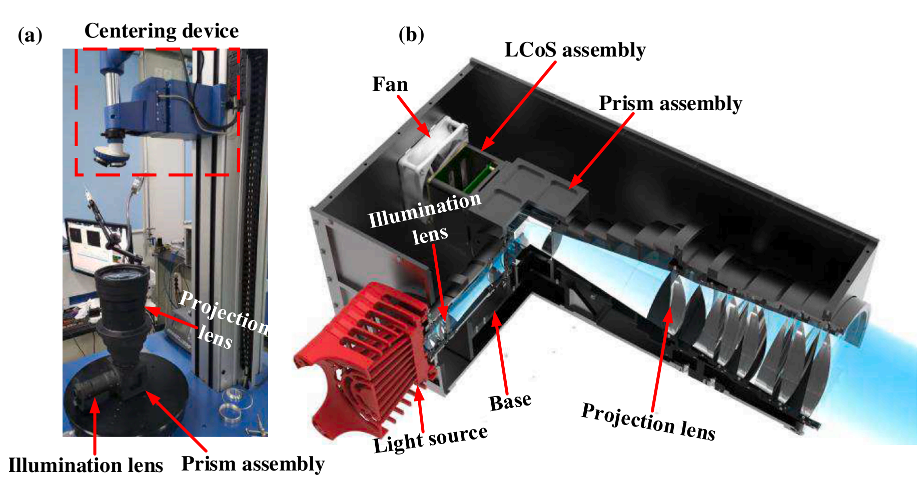

Fig. 6. (a) Assembly and alignment of the SFS. (b) Opto-mechanical system of the SFS.

4. Opto-thermal analysis of the SFS

The ambient temperature for the testing was different from that for the assembly, and the former changed in a predictable range of 10 to 35 °C. Furthermore, the power of the light source was 3 W and the illumination lens was heated after continuous irradiation. Except for the spacers, other critical mechanical parts were made of titanium (TC4). The coefficient of thermal expansion (CTE) of TC4 was close to that of a glass material, which could alleviate the influence of known thermal conditions on the optical performance. To further verify the thermal adaptability, an FEA model of the SFS was built for predicting the thermally induced displacements of nodes on the optical surface.

The coating on the optical element absorbed approximately less than 0.5 % incident energy, which was converted into heat. The temperature distribution inside the optical element or mechanical part depended on heat exchanging with ambient air and heat conduction. Both the source and LCoS chip were equipped with fans, which could only reduce the local temperature. Therefore, the thermal exchange between the opto-mechanical system and the environment relied on natural cooling, the convection heat coefficient of which was set to 10 W/m^2•℃. Furthermore, the radiant emissivities of glass and metal with black coating were assumed to be 0.93 and 0.95, respectively. The net incident energy was equal to the difference between the incident and emitted energy, which caused the temperature gradient in the solid. The initial temperature was set to 20 ℃ that is the assembly temperature. In addition, vertical and lateral loadings were applied to the threaded mounting holes of the base plate analogous to the connection between the SFS and FMS. Based on the above parameters and conditions, the solved temperature distribution of the SFS is shown in Fig. 7. Due to the existence of the heat source, the temperature distribution shows a trend of gradual decrease along the optical axis. Moreover, the non-uniform distribution is caused by heat exchange with the surroundings.

When the temperature fields were applied to the meshing model, the thermal strain built up and caused the displacements of nodes, which are shown in Fig. 8. The maximum displacement at 10℃ is 0.0409 mm, and the areas with large displacements are mainly concentrated on the outside of the opto-mechanical system. This trend is consistent with the temperature distribution. Therefore, it can be inferred that heat exchange with the surroundings is the primary factor driving the thermally induced displacements of nodes. The values of the material properties used in the FEA are listed in Table 2.

There were two reasons for the displacement of nodes on the optical elements. The first was the surface deformation, and the second was the lens movement caused by the deformation of the mechanical parts. Therefore, the actual surface deformation was smaller than the displacement. However, the maximum displacement of the opto-mechanical system at 40 ℃ approached 0.1 mm, and the maximum displacement of the optical elements was greater than 0.06 mm, which was unacceptable. An elastomer made of room temperature vulcanized silicone rubber (RTV) was used to fix the lens in the cell. To be athermal in the radial direction, the elastomer required a particular thickness. Furthermore, the mass of the lens in the projection module was large; thus, it was necessary to evaluate the decentration caused by the radial gravitational loading [34]. The calculated values of the thickness (t_e) and decentration (Δ_{lens}) are shown in Fig. 9. The actual value of t_e should be greater than or equal to the calculated result; thus, in practice, values less than 0.1 mm were specified as 0.1 mm. The maximum value of Δ_{lens} was 0.0004 mm, which proves that the decentration caused by gravitational loading can be ignored.

To verify the function of the elastomer, a comparative analysis was carried out at 40 ℃. When there was no elastomer, the displacements of the lens edge area were between 0.04 and 0.07 mm and the minimum displacement (0.0073 mm) occurred in the central area, as shown in Fig. 10(a). The calculated t_e value corresponding to this lens was approximately 0.3 mm. It can be seen from Fig. 10(b) that the displacements of the edge area decreased to the range of 0.006 to 0.008 mm and the displacement of the central area was halved. Compared with the case without an elastomer, the improvement of the temperature adaptability was significant. When the t_e value was further increased to 0.6 mm, the displacements of nodes did not continue to decrease but increased slightly, as shown in Fig. 10 (c). Due to the different CTEs, the axial lengths of the cell, elastomer, and lens changed at different rates along with the temperature. The shear was introduced into the elastomer, and its negative effect was amplified with the increase in t_e. In summary, as a radial athermal method, the actual t_e value should be as close as possible to the calculated result.

For evaluating the projection optical performance under specified thermal conditions, the thermally induced displacements were transformed into values of surface sag change [35], which can be expressed by:

$$Z \times A = \Delta S \tag{2}$$

where Z is an $m \times n$ matrix composed of Zernike polynomials, m represents the number of sampling nodes, n represents the number of terms, A is the column vector composed of Zernike coefficients, and ΔS is the column vector composed of surface sag changes. Common solution algorithms of Zernike coefficients include the least squares method, Gram-Schmidt orthogonalized method, Householder transformation, and SVD. Among them, the SVD can effectively avoid the ill-conditioned problem and improve the efficiency and accuracy of the solution. Based

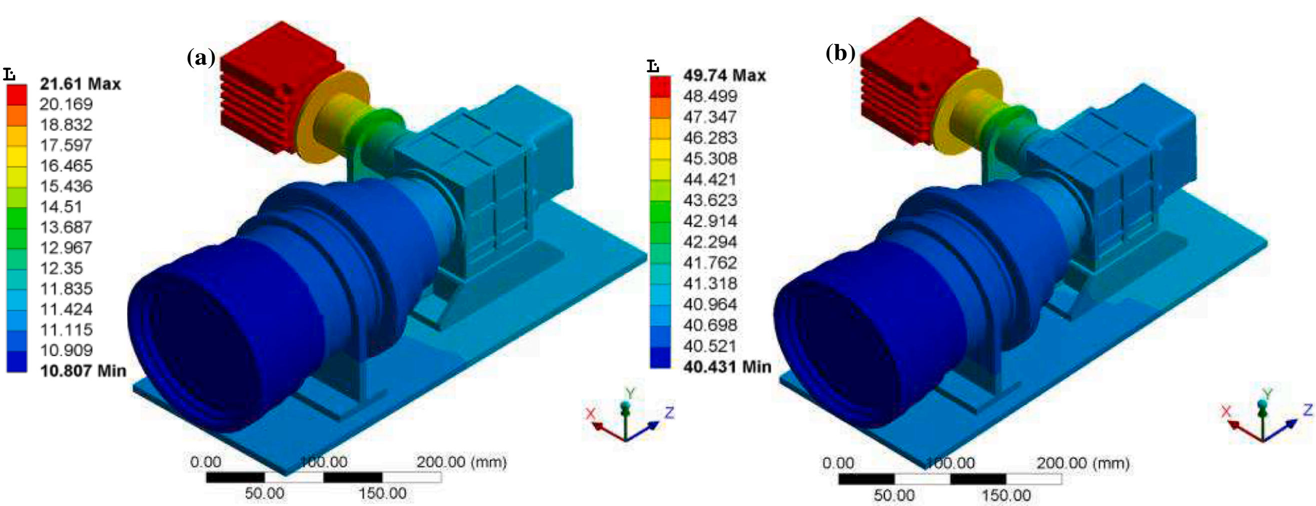

Fig. 7. Temperature distribution of the SFS. (a) Ambient temperature of 10 ℃. (b) Ambient temperature of 40 ℃.

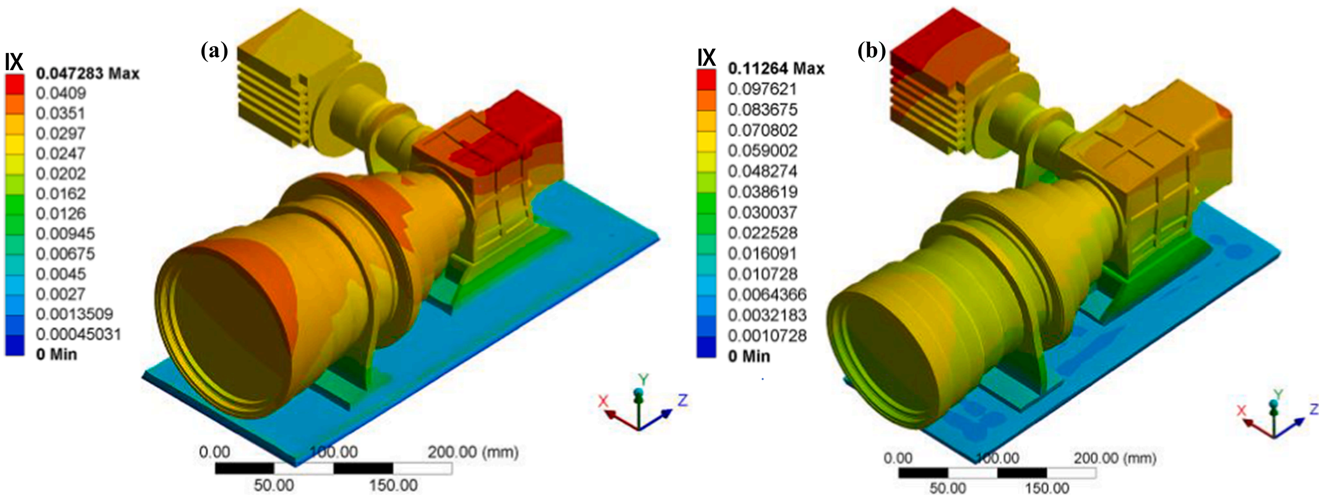

Fig. 8. Displacement distribution of the SFS. (a) Ambient temperature of 10 ℃. (b) Ambient temperature of 40 ℃.

Table 2
Material properties used in the FEA.

Component	Material	Conductivity (W/m•K)	CTE (℃$^{-1}$)	Young's modulus (GPa)	Density (g•cm^{-3})	Specific heat (J/kg•K)	Poisson's ratio
Lens 1	B270	0.92	9.4×10^{-6}	71.5	2.55	860	0.219
Lenses 2,4,5,6	NBK7	1.11	7.1×10^{-6}	82	2.51	858	0.206
Lens 3	Fused Silica	1.40	0.58×10^{-6}	7.3	2.20	741	0.170
Lenses 7,9,12,13	H-FK61	0.73	13.01×10^{-6}	71	3.7	670	0.298
Lenses 8,11	H-LaK52	0.82	5.81×10^{-6}	117	4.02	520	0.290
Cell, Barrel	TC4	7.3	8.8×10^{-6}	114	4.43	611	0.34
Elastomer	RTV	1.2	248×10^{-6}	0.0034	1.22	–	0.49

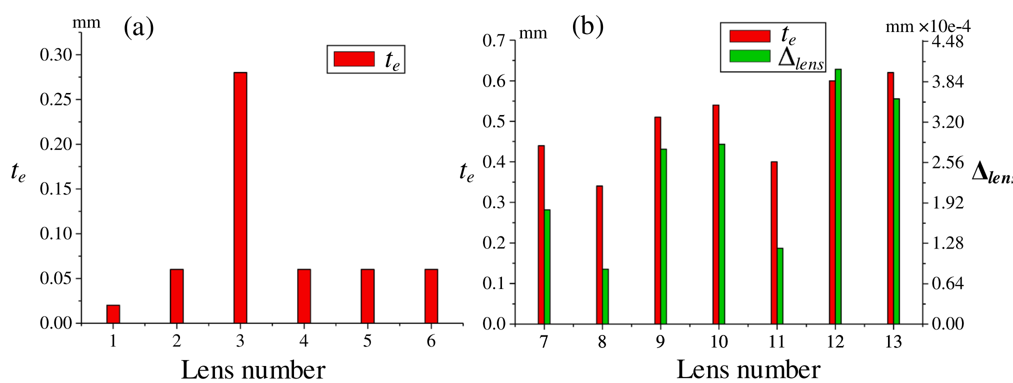

Fig. 9. Calculation results of t_e and Δ_{lens}. (a) The illumination lenses. (b) The projection lenses.

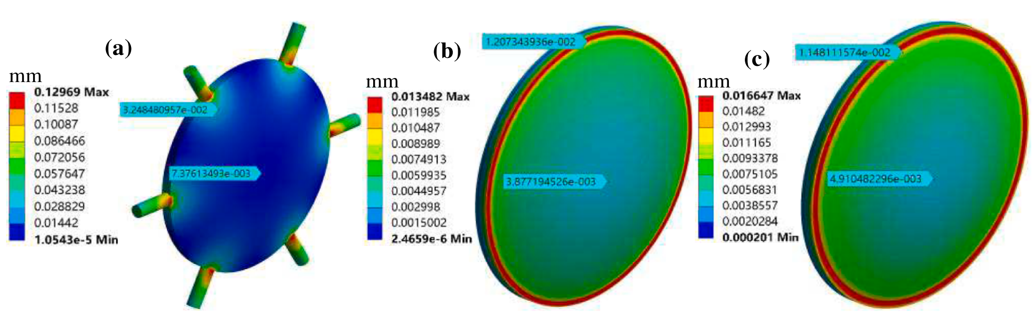

Fig. 10. Thermally-induced displacements of nodes against different elastomer thicknesses. (a) No elastomer. Cylinders represented RTV injected into threaded holes. (b) Elastomer thickness of 0.3 mm. (c) Elastomer thickness of 0.6 mm.

on the rules of SVD, Z can be decomposed by:

$$Z = U\begin{bmatrix}\Sigma\\0\end{bmatrix}_{m\times n}V^T \tag{3}$$

where U is an $m \times m$ orthogonal matrix, the column vectors of which are the feature vectors of AA^T; V^T is an $n \times n$ orthogonal matrix, the column vectors of which are the feature vectors of A^TA; and Σ is a diagonal matrix composed of singular values of A.

The least squares solution of Eq. (2) is expressed as:

$$\|ZA - \Delta S\|_2^2 = \left\| U\begin{bmatrix}\Sigma\\0\end{bmatrix}V^TA - \Delta S\right\| = \left\|\begin{bmatrix}\Sigma\\0\end{bmatrix}V^TA - U^T\Delta S\right\| \tag{4}$$

The first n column vectors of U are used to form a new matrix $U_{m\times n}$, and U is defined as:

$$U = \left[U_{m\times n}, U_{m\times(m-n)}\right] \tag{5}$$

Eq. (4) can then be expressed as:

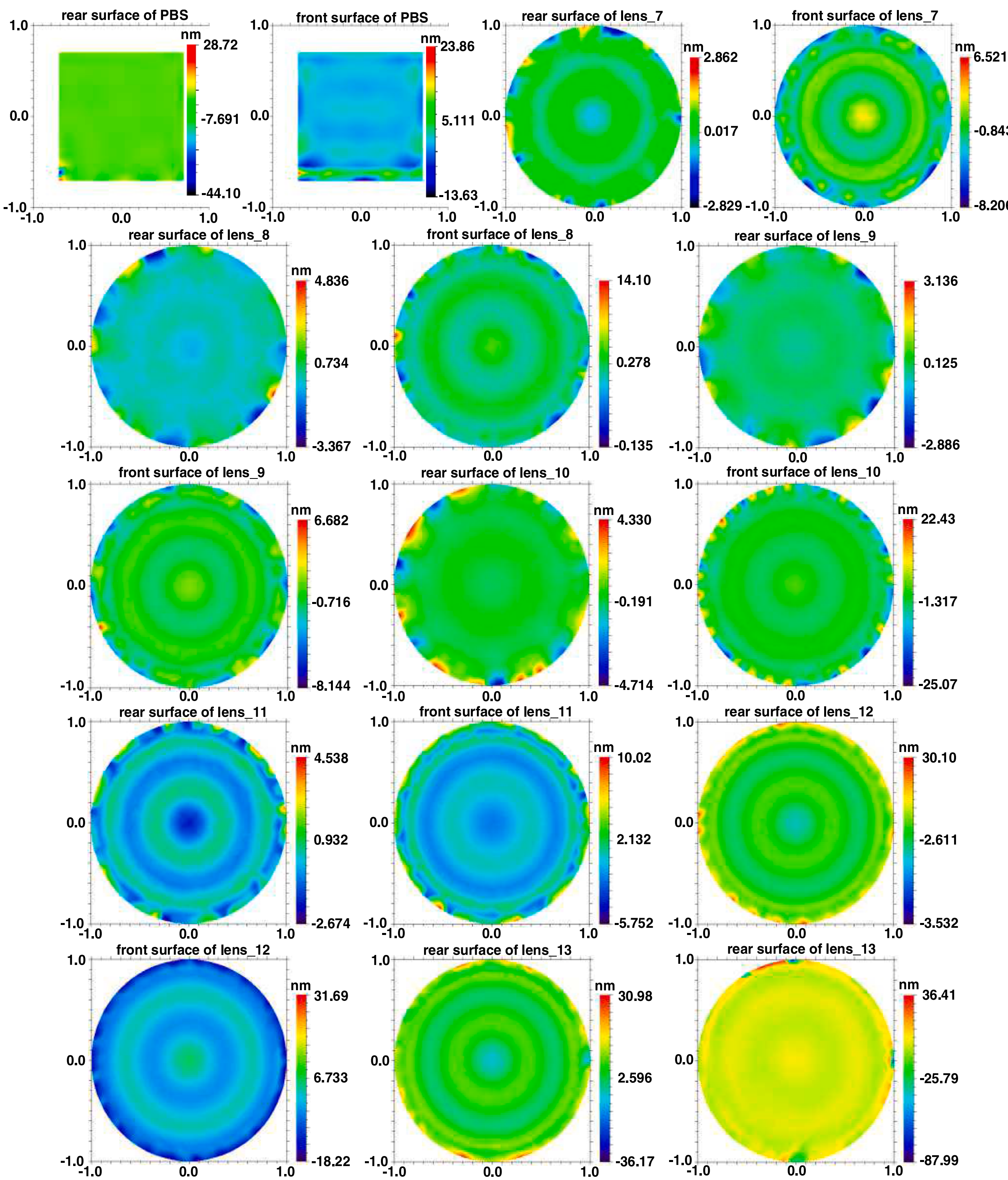

Fig. 11. Residual maps of all optical surfaces. The surface close to the LCoS chip is regarded as the rear surface of the PBS. All images are arranged in order.

$$\|ZA-\Delta S\|_2^2 = \left\|\Sigma V^T A - U^T_{m\times n}\Delta S - U^T_{m\times(m-n)}\Delta S\right\| \tag{6}$$

According to the matrix decomposition, the right side of Eq. (6) can be transformed into

$$\left\|\Sigma V^T A - U^T_{m\times n}\Delta S\right\| + \left\|U^T_{m\times(m-n)}\Delta S\right\| \geq \left\|U^T_{m\times(m-n)}\Delta S\right\| \tag{7}$$

When $\left\|\Sigma V^T A - U^T_{m\times n}\Delta S\right\| = 0$, the minimum value is obtained for Eq. (6). According to this condition, Zernike coefficients are solved by

$$A = \left(\Sigma V^T\right)^{-1} U^T_{m\times n}\Delta S = V\Sigma^{-1}U^T_{m\times n}\Delta S \tag{8}$$

Based on the above algorithm, MATLAB was used to compute Zernike coefficients for all optical surfaces in the projection module, including 16 surfaces in total. To effectively visualize small-scale surface elevations, the Zernike reconstructed surface was subtracted from the original sag data. The corresponding residual maps of all the optical surfaces are shown in Fig. 11. It is commonly considered that Zernike polynomials are effective in capturing low-frequency imperfections, which means that the fitting accuracy will not be improved with the increase in the total number of Zernike terms. Accordingly, only the first 37 Zernike terms were used in the fitting process. There are evident fluctuations along the edge of the lens. These areas are located at opto-mechanical interfaces, and the displacements of nodes are seriously affected by mechanical parts. However, these areas are outside the effective aperture of the lens, having no influence on the image quality. Residual maps clearly show the thermal print-through phenomenon, which is essentially caused by the axial thermal loading. As for a large reflective-type optical system operating in a thermally dynamic environment, a lightweight designed mirror structure can mitigate the impact of this phenomenon; however, this is not achievable for the transmissive-type system.

5. Preliminary assessment of the SFS

All undeformed surfaces were spherical in the projection lens; thus, the deformed surfaces can be expressed as:

$$s = \frac{c\rho^2}{1+\sqrt{1-(K+1)c^2\rho^2}} + \sum_{j=1}^{37} a_j Z_j(\rho,\varphi) \tag{9}$$

where s is the sag of the deformed surface, c is the vertex curvature, and K is the conical degree. In Eq. (9), the former represents the nominal surface and the latter represents the sag change determined by Zernike polynomials.

The standard Zernike polynomials were selected to estimate sag change data and the solved Zernike coefficients of all deformation surfaces were directly imported into the projection optical model built using ZemaX ray-tracing software. The thermally induced deformations were assumed to worsen when the ambient temperature reached its minimum or maximum value. The MTF was used to evaluate the projection optical performance, as shown in Fig. 12.

As shown in Fig. 12 (a) and (b), the MTF values were all greater than 0.4 at 61C/mm (cycles per mm), which implies that the decreasing temperature has minimal influence on the optical performance. When the temperature was increased to 30 ℃, except for the edge field, the MTF values of other fields were still greater than 0.4, as shown in Fig. 12 (c). However, when the temperature continued to rise to 40 ℃, the MTF value of the edge field declined to below 0.3. The changing trend of the MTF curves shows that the rising temperature is the prime factor compromising the optical performance. Even if the CTE of TC4 was close to that of a glass material, forced cooling was required along with a continuously rising temperature. To ensure the optical performance of the SFS under natural air circulation, the ambient temperature should be stabilized below 40 °C, which should be lower for infrared optical systems, based on preceding studies.

The wavefront performance of the assembled SFS was measured using an interferometer. The source wavelength of the interferometer was 632.8 nm, which was selected as the reference. The peak-to-valley (PV) and root mean square (RMS) of the design wavefront are 0.2767 λ and 0.0802 λ, respectively, for the central field, as shown in Fig. 13(a). Compared with the design, the measured result in Fig. 13(b) shows that the PV is 0.425 λ, twice the design value. However, the deviation of RMS from the design is less than 0.02λ, which is sufficient to confirm that the assembly and alignment are excellent.

The interferometer was mainly used to record the phase information

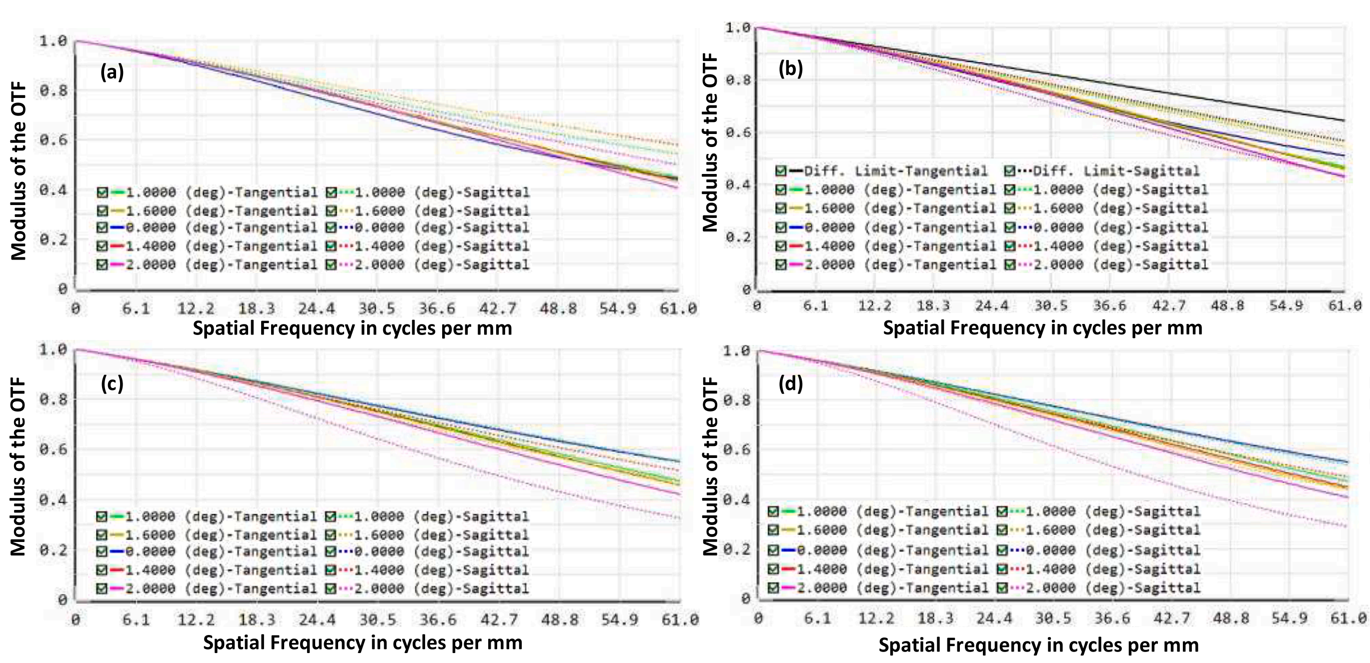

Fig. 12. MTF curves of the projection module (a) at 10 °C, (b) at 20 °C, (c) at 30 °C, and (d) at 40 °C, in which 20 ℃ is the standard temperature. MTF values are equal to the modulus of the optical transfer function (OTF).

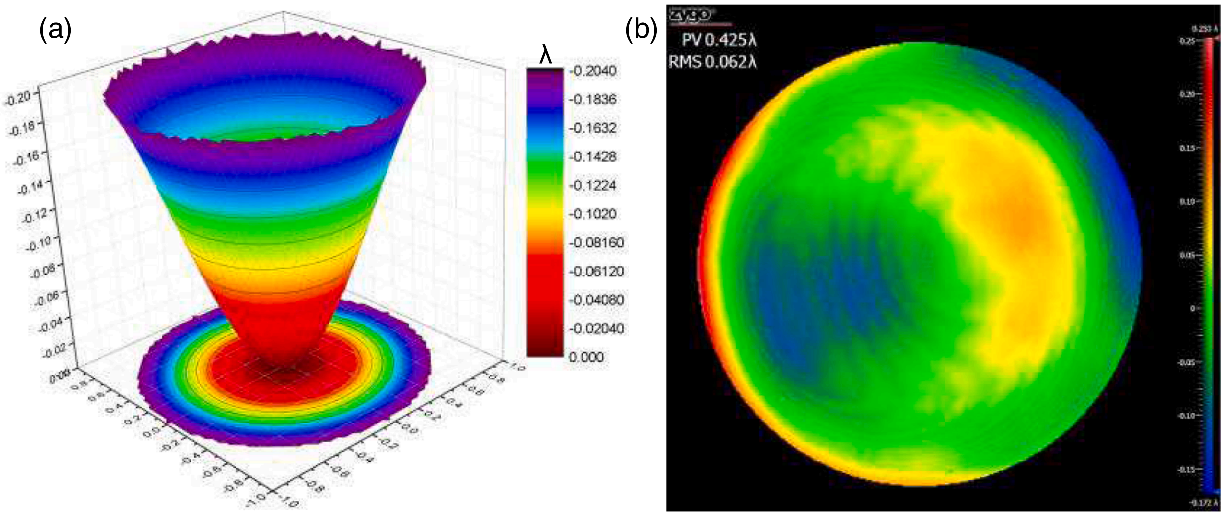

Fig. 13. Wavefront error of the center field at 632.8 nm. (a) Design result. (b) Interferogram.

Table 3
Coefficients of residual Zernike aberration terms of design and measurement results.

	ZFR1: −0.159	ZFR4: −0.138	ZFR9: 0.021		
Design result[a]	1 	$2\rho^2$-1 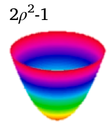	$6\rho^4$-$6\rho^2+1$ 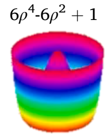	- -	
	ZFR5: −0.015 $\rho^2\cos(2\varphi)$	ZFR6: −0.028 $\rho^2\sin(2\varphi)$	ZFR7: −0.15 ($3\rho^3$-2ρ)$\cos\varphi$	ZFR8: −0.0053 ($3\rho^3$-2ρ)$\sin\varphi$	ZFR9: 0.0336 $6\rho^4$-$6\rho^2+1$
Measurement result		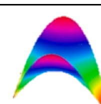	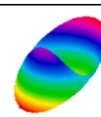	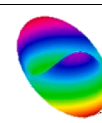	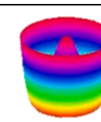

[a] The fringe Zernike polynomials contain 37 terms in total, only the first 9 terms of which are utilized by the interferometer.

of the wavefront; thus, the wavefront aberrations were more suitable to be expressed by fringe Zernike polynomials. The coefficients of residual Zernike aberration terms are listed in Table 3.

As shown in Table 3, the residual terms of the design result correspond to the piston, defocus, and primary spherical, in which the defocus and piston terms are dominant. As the piston term do not change the shape of the wavefront, Fig. 13 (a) is very similar to the defocus term. The purely radial terms all exhibit axisymmetry, no matter which term is dominant, as the wavefront shows the same characteristics. Furthermore, a very small amount of secondary and tertiary spherical aberrations existed in the design result, and their Zernike coefficients were 0.000033 and 0.00000026, respectively, which can be ignored. For the measurement result, all mixed terms contain radial and angular parameters, except for the primary spherical term, including two types of primary astigmatism and coma. Other terms are approximately 1-order smaller than the seventh term that represents the primary coma-A, resulting in strong asymmetry, as shown in Fig. 13 (b).

The single star position error and angular distance error between stars are two important parameters to evaluate the quality of the SFS. Many previous studies introduced the correction method for the former, which usually used a theodolite to measure the azimuth and elevation angles of reference star points and calculated their real coordinates. The correction coefficient of each reference star can be calculated to further

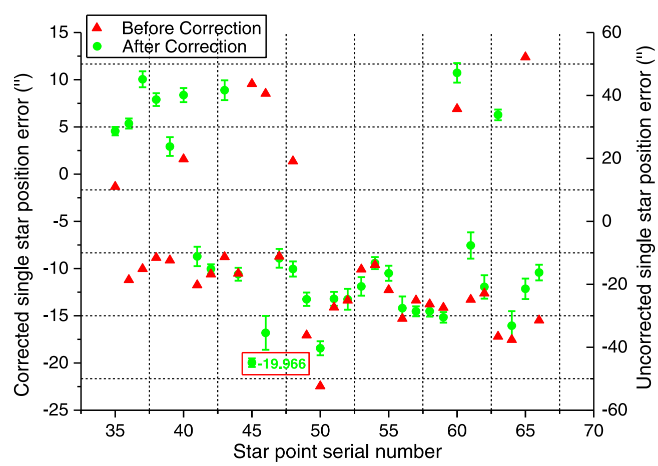

Fig. 14. Single star position error. The maximum is highlighted by the rectangular box.

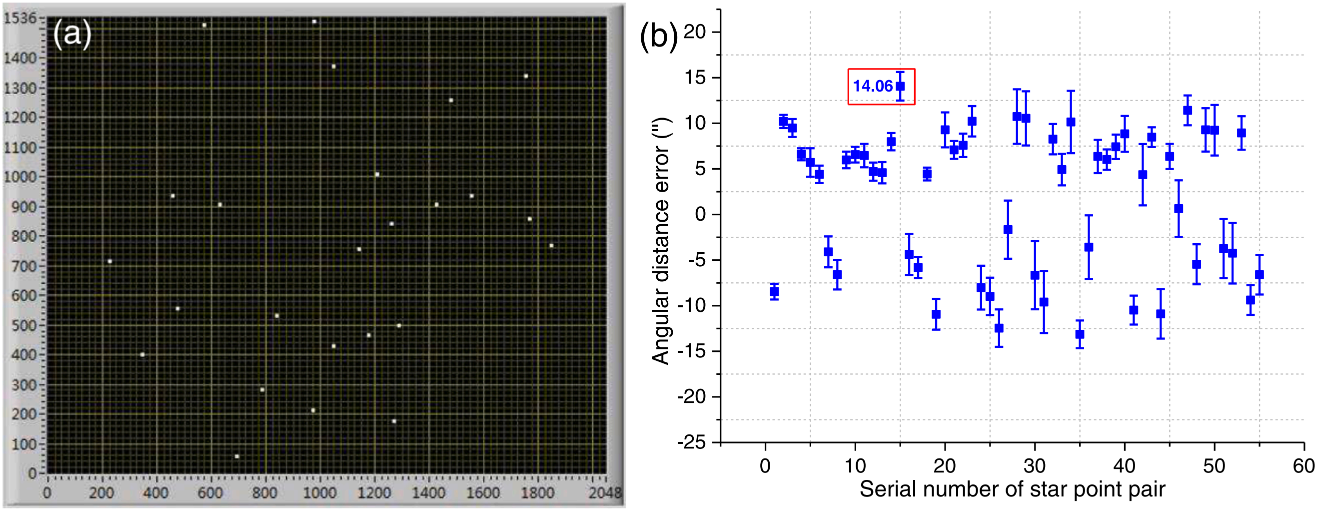

Fig. 15. Measurement of the angular distance error between stars. (a) A sample star map. (b) Measurement result. The maximum is highlighted by the rectangular box.

obtain the relationship between the correction coefficient and star coordinate, thus ensuring that the star point is projected to the right position [36]. Applying these steps, each point was measured five times. The average and standard deviation of these five values were calculated. The corrected single star point position errors are stable within 20″ with a standard deviation of 0.45″. The corrected and uncorrected data of reference points are plotted in Fig. 14.

The information from several star maps was uploaded to the LCoS chip to measure the angular distance error between stars, as shown in Fig. 15(a). A star point was represented by 3 × 3 pixels, and the active area of the LCoS chip was meshed according to the spatial resolution. The angular distance error between two arbitrary points can be expressed by:

$$\sigma = \arccos[\cos(\alpha_1-\alpha_2)\cos(\beta_1-\beta_2)] - \arccos\left[\frac{f}{\sqrt{p^2\left[(a_1-a_2)^2+(b_1-b_2)^2\right]+f^2}}\right] \tag{10}$$

where (a_1, b_1) and (a_2, b_2) represent the coordinates of two points displayed on the LCoS, p is the pixel pitch, f is the actual projection focus length, (α_1, β_1) and (α_2, β_2) represent the azimuth and elevation angles of two points measured by the theodolite, respectively. Similarly, each star point pair was measured five times. It can be seen from Fig. 15(b) that the maximum average error is 14.06″ (the corresponding standard deviation was 1.56″), which is in accordance with the design specifications.

6. Conclusion

This study on a dynamic SFS began in late 2019. The original approach was to use a secondary imaging optical architecture to achieve an ultra-long exit pupil distance, broad waveband, and zooming function. Due to the strict limitations of the reserved space of the FMS, the original design was abandoned. The design discussed and evaluated in this study was the latest practical system, removing the effect of the zooming function. The opto-mechanisms closed-loop design comprehensively considered stray light suppression, assembly, and alignment along with thermal adaptability. In addition to the material selection and structural optimization, a detailed FEA model was used to evaluate the thermally induced displacements of nodes on optical surfaces. Furthermore, the optical performance of the SFS under different thermal conditions was analyzed by Zernike polynomials and sequential ray-tracing, verifying the effectiveness to be below 40 ℃. The laboratory test and calibration showed that the PV and RMS of the SFS wavefront were 0.425 λ and 0.062 λ, respectively, the single star point position errors were concentrated within 20″, and the angular distance errors between stars were less than 15″. The potential of the SFS used for the large FMS was proven by these results. Apart from testing the STR, the SFS could also project various scene images to test other imaging devices such as the airborne camera. Given the scarcity of existing research on opto-thermal analysis for transmissive-type systems, the approach presented in this study helps design similar systems requiring high-temperature adaptability. In the future, the conversion of unpolarized light to s-polarized light can be further explored to improve the SFS optical efficiency.

Declaration of Competing Interest

The authors declare that they have no known competing financial interests or personal relationships that could have appeared to influence the work reported in this paper.

Data availability

Data will be made available on request.

Acknowledgments

The authors acknowledge the National Natural Science Foundation of China (61605016) and the Education Department of Jilin Province (JJKH20210824KJ).

References

[1] Y. Ni, D. Dai, W. Tan, X. Wang, S. Qin, Attitude-correlated frames adding approach to improve signal-to-noise ratio of star image for star tracker, Optics Express 27 (11) (2019) 15548–15564.
[2] T. Sun, F. Xing, X. Wang, Z. You, D. Chu, An accuracy measurement method for star trackers based on direct astronomic observation, Scientific Reports 6 (2016) 22593.
[3] E. López-Fraguas, J.M. Sánchez-Pena, R. Vergaz, A low-cost LED-based solar simulator, IEEE Transactions on Instrumentation and Measurement 68 (12) (2020) 4913–4923.
[4] Victor Hugo Schulz, Gabriel Mariano Marcelino, Laio Oriel Seman, Jeferson Santos Barros, Sangkyun Kim, Mengu Cho, Gabriel Villarrubia González and Valderi Reis Quietinho Leithardt, and Eduardo Augusto Bezerra, "Universal verification platform and star simulator for fast star tracker design", Sensors **21**, 907 (2021).
[5] Jinyun Yan, Jie jiang, and Guangjun Zhang, "Dynamic imaging model and parameter optimization for a star tracker", Optics Express **24**(6), 5961-5983 (2016).

[6] G. Li, R.u. Lingyun Wang, X.Y. Zheng, Y. Ma, X. Liu, B.o. Liu, Research on partitioning algorithm based on dynamic star simulator guide star catalog, IEEE Access 9 (2021) 54663–54670.
[7] M.A. Samaan, S.R. Steffes, S. Theil, Star tracker real-time hardware in the loop testing using optical star simulator, Proc. Space Flight Meeting 2233–2245 (2011).
[8] N. Filipe, L. Jones-Wilson, S. Mohan, K. Lo, W. Jones-Wilson, Miniaturized star tracker stimulator for closed-Loop testing of CubeSats, Journal of Guidance, Control, and Dynamics 40 (12) (2017) 3239–3249.
[9] G. Rufino, D. Accardo, M. Grassi, G. Fasano, A. Renga, U. Tancredi, Real-time hardware-in-the-loop tests of star tracker algorithms, International Journal of Aerospace Engineering 2013 (2013), 505720.
[10] Z. Jianzhong, S. Qiang, Y. Le, W. Jian, L. Ying, L.i. Chun, Design of LCD-based visible scene simulator with long exit pupil relief and large field of view, Infrared and Laser Engineering 41 (9) (2012) 2454–2458.
[11] Z. Xiong, H.a. Liu, X. Tan, L.u. Zhenwu, C. Li, L. Song, Z. Wang, Diffraction analysis of digital micromirror device in maskless photolithography system, Journal of Micro/Nanolithography, MEMS, and MOEMS 13 (4) (2014), 043016.
[12] X.-Y. Ding, Y.-X. Ren, L. Gong, Z.-X. Fang, L.u. Rong-De, Microscopic lithography with pixelate diffraction of a digital micro-mirror device for micro-lens fabrication, Applied Optics 53 (24) (2014) 5307–5311.
[13] X. Chen, B.-B. Yan, F.-J. Song, Y.-Q. Wang, F. Xiao, K. Alameh, Diffraction of digital micromirror device gratings and its effect on properties of tunable fiber lasers, Applied Optics 51 (30) (2012) 7214–7220.
[14] H. Ryoo, D.W. Kang, J.W. Hahn, Analysis of the effective reflectance of digital micromirror devices and process parameters for maskless photolithography, Microelectronic Engineering 88 (3) (2011) 235–239.
[15] Y.u. Dai, C. Xin, Z. Wenming, L.i. Jie, L. Shenglin, Design of optical system based on DMD for simulator with large field of view and long exit pupil distance, Journal of Applied Optics 41 (5) (2020) 892–897.
[16] J.-W. Pan, H.-H. Wang, High contrast ratio prism design in a mini projector, Applied Optics 52 (34) (2013) 8347–8354.
[17] W.-S. Sun, C.-L. Tien, C.-H. Ma, J.-W. Pan, Compact LED projector design with high uniformity and efficiency, Applied Optics 53 (29) (2014) H227–H232.
[18] J. Yi, P. Zhao-Xin, Y.u. Yang, Design of optical engine for infrared scene simulation system based on DMD, Journal of Infrared and Millimeter Waves 33 (4) (2014) 376–379.
[19] W.-S. Sun, J.-W. Pan, Non-telecentric projection lens design for an LED projector, Applied Optics 56 (3) (2017) 712–720.
[20] Y. Pan, X.u. Xiping, Y. Qiao, Design of two-DMD based zoom MW and LW dual-band IRSP using pixel fusion, Infrared Physics & Technology 91 (2018) 90–100.
[21] Z. Han, B. Yan, Y. Qi, Yanwei Wang and Yu Wang "Color holographic display using single chip LCoS", Applied Optics 58 (1) (2019) 69–75.
[22] M. Carmen García-Domene, M. José Luque, D. de Fez, The problem of spatial homogeneity in an LCoS projector, Optik 198 (2019), 163252.
[23] M. Yao, Z. Guo-Yu, S. Gao-Fei, L. Shi, Z. Yun-Shuai, Optimal Design of Optical Engine for Star Simulators Based on LCoS Splicing, Acta Photonica Sinica 46 (3) (2017) 0312002.
[24] F.u. Jing-Yi, Q. Tian-Xiang, H. Yun-Han, L. Zhi-Ying, A field of view splicing method for the optical system of a star simulator, Chinese Optics 14 (6) (2021) 1469–1475.
[25] E. Chen, P. Liu, Y.u. Feihong, Synchronized parameter optimization of the double freeform lenses illumination system used for the CF-LCoS pico-projectors, Optics & Laser Technology 44 (7) (2012) 2080–2087.
[26] Y. Pan, H.u. Mai, X.u. Xiping, Y. Qiao, Opto-mechanical temperature adaptability analysis of a dual-band IRSP for HWIL simulation, Infrared Physics & Technology 105 (2020), 103164.
[27] D. Dipasquale, S. Debei, G. Cremonese, F. Capaccioni, P. Palumbo, Optical performance evaluation of the high spatial resolution imaging camera of BepiColombo space mission, Optics and Laser Technology 141 (2021), 107172.
[28] Z. Li, B.o. Chen, K. Song, X. Wang, S. Liu, L. Yang, H.u. Qinglong, K.e. Qiao, L. Zhang, W.u. Guodong, Y.u. Ping, Opto-mechanisms design of extreme-ultraviolet camera onboard Chang E lunar lander, Optics Express 22 (13) (2014) 15932–15940.
[29] M. Zhang, L.u. Qipeng, H. Tian, D. Wang, C. Chen, X. Wang, Design and optimization for mounting primary mirror with reduced sensitivity to temperature change in an aerial optoelectronic sensor, Sensors 21 (2021) 7993.
[30] M. Shao, L. Zhang, X. Jia, Optomechanical integrated optimization of a lightweight mirror for space cameras, Applied Optics 60 (3) (2021) 539–546.
[31] Y. Bai, J. Li, R. Zha, Y. Wang, G. Lei, Catadioptric optical system design of 15-magnitude star sensor with large entrance pupil diameter, Sensors 20 (2020) 5501.
[32] E.C. Fest, Stray Light: Analysis and Control, (SPIE Press, 2013, p. Chap. 9..
[33] Liyin Yuan, Jianan Xie, Zhiping He, Yueming Wang, and Jianyu Wang, "Optical design and evaluation of airborne prism-grating imaging spectrometer", Optics Express **27**(13), 1786–1770 (2019).
[34] T.M. Valente, R.M. Richard, Interference fit equations for lens cell design using elastomeric lens mountings, Optical Engineering 33 (4) (1994) 1223–1228.
[35] R.K. Banyal, B. Ravindra, S. Chatterjec, Opto-thermal analysis of a lightweighted mirror for solar telescope, Optics Express 21 (6) (2013) 7065–7081.
[36] L.i. Guangxi, W. Lingyun, R.u. Zheng, M.a. Yue, L. Xiao, Research on correction method of star point position error of dynamic star simulator, Optik 241 (2021), 167017.